Enhanced Electrochemical Hydrogen Evolution of WTe$_2$ by Introducing Te vacancies

Wanying Lin, Biao Zhang, Jun Jiang, Liying Ma[*]

School of materials science and engineering and Tianjin Key Laboratory of Composites and Functional Materials, Tianjin University, Tianjin 300350, China
[*]E-mail: lyma@tju.edu.cn (L.Y. Ma)

Developing efficient, cost-effective and earth-abundant electrocatalytic materials for hydrogen evolution reaction (HER) is strategically important to realize sustainable development. HER in alkaline media is imperative for the hydrogen supply in commercial applications. However, transition metal dichalcogenides (TMDs) have been validated to be eminently propitious to acid HER, instead of alkaline solutions. It still remains challenging to design effective TMDs electrocatalysts towards alkaline HER rationally. This study gives a description of gearwheel-like WTe$_2$ nanomaterials with induced anionic (Te) vacancies which affords an overpotential of 178 mV at current densities of 10 mA/cm^2 as well as a durable stability (with minor activity decay after the 15 h test) in alkaline HER.

1. INTRODUCTION

Since the increasingly polluted environment and the sharp decline of traditional fossil fuel are currently threatening human survival and development, the importance of exploiting green technology becomes prominent [1-3]. Renewable energy sources such as tidal energy and wind energy have been vigorously developed, and the increasing maturity of related technologies has created prospects for large-scale industrial applications. However, the energy utilization efficiency of renewable energy is intrinsically limited by the factors of geography or weather, which hastens humans to excavate more potential energy source for effective and sustainable use on industrial scale [4].

Being green technology, electrocatalysis makes use of sustainable resources (H$_2$O as the raw materials and renewable energy as the driving force) to churn out high value-added products (pure H$_2$ and O$_2$ suitable for fuel cells), which would be a boon for energy crunches and concerns about climate change [5]. The acidity and basicity of electrochemical catalysts might be the key factors influencing the

catalytic activities [6]. Generally, two primary steps involved in acid HER are Volmer step and Heyrovsky step (maybe Tafel step). The HER activity is higher in acid electrolytes because it contains a large amount of ready-made reactant H^+ [5,7]. However, there are certain shortcomings in acid electrolyzer, such as the acid mist generated by electrolyte and the rapid corrosion effect on the electrolyzer [8,9]. In this regard, various tactics have been instigated to unveil the mechanism in alkaline systems.

In contrast to acid HER, the alkaline HER process is more complicated: water dissociation to produce OH^- and H^+ ions ($H_2O+ * \rightarrow H^+ + OH^-$, * denotes the catalysts) first happens in alkaline electrolyzers. It is strenuous to break the H-O bond to yield H^+, which signify the cumbersome reaction kinetic in alkaline system [9-12]. Hence, massive endeavours have been developed to manipulate the structure of catalyst in order to achieve an optimal ΔG_{H*} in alkaline electrolyte [13]. It is well known that platinum (Pt)-based catalyst is the most ideal HER catalyst up to now, but essentially impeded by its high price and earth scarcity in practical engineering [14]. Recently transition metal dichalcogenides (TMDs) have magnetized substantial concentration for the reason of their affordability, availability and polymorphism [15, 16]. Most common polymorphs of group VI TMDs are 2H and 1T/1T' phase, among which 2H phase displays semiconducting property, while 1T/1T' phase displays metallic or semimetallic property [17]. In terms of the aquatic hydrogen electrolysis, for example, the active sites of MoS_2 with 2H being the thermodynamically stable phase locate at the unsaturated atoms of edge. The majority of its basal surface remains catalytically inert to HER [18]. By comparison, the thermodynamically stable phase of WTe_2 is semimetallic 1T' phase (the slightly distorted 1T phase), a big difference from the 2H phase of other group VI TMDs. The active sites of WTe_2 are locate at basal plane rather than edges [19-22]. The larger interplanar lattice spacing attributes to weak van der Waals force, which is conducive to rapid mass penetrance [23-25]. Thus, the favorable electrical conductivity and electrochemical properties make WTe_2 quite suitable for HER. Moreover, the weak interlayer bonding energy and two-dimensional (2D) structure endow WTe_2 with a larger surface area and a rapid diffusion of ions, which is optimum for HER activity. All these advantages enable WTe_2 to perform well as a HER catalyst [26-28]. Wang et al. found that the oxygen plasma results in a large amount of tungsten vacancies on WTe_2 nanosheets, which shows an overpotential of 251 mV at 10 mA/cm^2, much lower than that of pristine nanosheets [29]. Kwon et al. induced a spot of Te vacancies on the surface of WTe_2 by high-temperature vacuum-annealing, which increasing the conductivity and the electrochemical active surface area, thus displays excellent HER performances [20].

In this study, using WTe_2 as the research model, we optimized the alkaline HER performance of WTe_2 supported on carbon cloth by introducing Te vacancies (WTe_{2-x}/ CC) by thermal reduction in vacuum. Te-deficient WTe_{2-x} displays 178 mV overpotential at 10 mA/cm^2 in 1M KOH, a small Tafel slope of 151 mV/dec, and no obvious degradation after the 15 h stability test.

2. EXPERIMENTS

2.1. Materials

All chemicals in present experiments were used as received from commercial sources without

further treatment. Sodium tungstate (Na_2WO_4, AR) was purchased from Kermel CO., Ltd. Nitric acid (HNO_3) was obtained from Tianjin Jiangtian Chemical Reagent Factory. Potassium permanganate ($KMnO_4$, AR) was acquired from Tianjin Damao Chemical Reagent Factory. Carbon cloth (WOS109) was purchased from CeTech Co., Ltd. Sodium hydroxide (KOH, 99.5%) was obtained from Kermel CO., Ltd, used for electrochemical measurement.
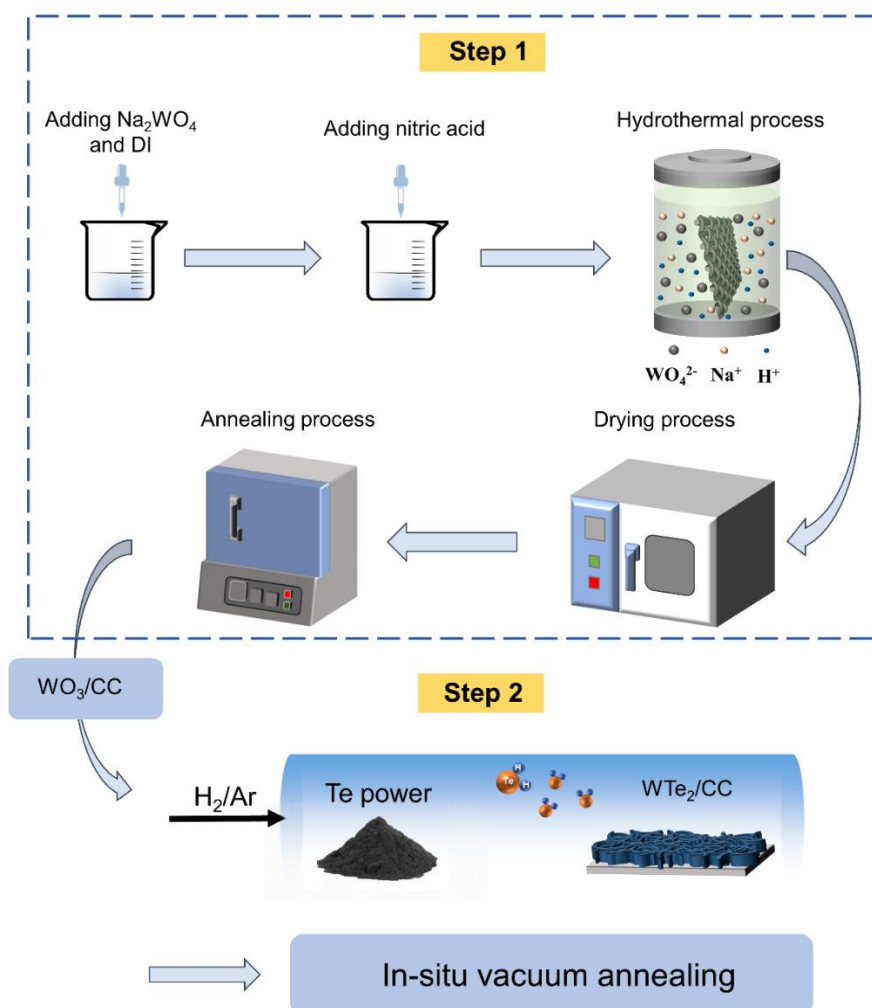
2.2. Synthesis

Figure 1. The fabrication process of WTe_{2-x} nanomaterials on carbon cloth.

2.2.1 Synthesis of WO_3 on carbon cloth

WO_3/CC was synthesized by hydrothermal method, as shown in Figure 1 (step1). Na_2WO_4 was dissolved in deionized water (DI) under stirring for 30 min. Afterward, HNO_3 solution was added dropwise with constant stirring meanwhile. The carbon cloth and the obtained solution were transferred into a autoclave of 50 mL capacity and kept heated at 180°C for 12 h hydrothermal treatment. The carbon cloth was immersed in solution and not adhered to the wall of the autoclave. After cooling down to room

temperature, the specimen was rinsed with deionized water and ethanol successively, followed by vacuum drying at 70°C overnight. Finally, WO_3/CC was achieved after annealing at 350°C for 2 hours to remove the crystal water of $WO_3 \cdot 6H_2O$ [30].

2.2.2 Synthesis of Te-deficient WTe_{2-x} on carbon cloth

As shown in Figure 1 (step2), pristine WTe_2/CC was synthesized by chemical vapor deposition (CVD) and WTe_{2-x}/CC was obtained by in-situ vacuum annealing. 1 g Te powder was put upstream and WO_3/CC was placed in the middle of the quartz tube. The quartz tube was flushed with ongoing Ar gas for 30 min to exhaust air, followed by setting of Ar (80 sccm) mixed with H_2 (30 sccm) flowing gas. Reaction temperature was slowly increased to 600°C and kept for 2 hours. Then the furnace was cooled down naturally. During the process, vaporized tellurium steam reacts with H_2 to form an intermediate product, H_2Te, which activate the conversion of WO_3 to WTe_2 despite the low enthalpy of formation [24]. With in-situ thermal reduction, WTe_2/CC were annealed at 80°C, 100°C, 200°C, 300°C respectively in 10^{-1} MPa to induce Te vacancies.

2.3. Materials characterizations

Scanning electron microscopy (SEM) images were recorded by Hitachi S4800 scanning microscope to analyze the microstructure. JEOL JEM-2010 was used to purchase Energy dispersive X-ray spectrum (EDS) mapping and operated at 200 kV. X-ray diffraction (XRD) patterns were excuted on Bruker D8 ADVANCE in the 2θ range from 10° to 90° to identify the phase composition. X-ray photoelectron spectroscopy (XPS) was collected on Kratos Axis Supra with a 45° take-off angle. LabRAM HR Raman spectrometer was used to gain Raman spectroscopy at an excitation wavelength of 532 nm. Paramagnetic resonance spectrometer (EPR, Bruker EMX PLUS) is used to capture single electronic signals and investigate the Te vacancies, the magnetic field of the test center was 3510 G, the scanning width was 100 G, the scanning time was 30 s, the microwave power was 2.0 mW and the modulation amplitude was 3 G.

2.4. Electrochemical characterizations

A typical three-electrode electrolyzer with a CHI660E electrochemistry workstation was used to examine the electrocatalytic performance at room temperature in 1M KOH. The obtained self-supportive electrode was applied to be the working electrode, along with a saturated calomel electrode (SCE, saturated KCl) as the reference electrode and a graphite rod as the counter electrode. All potentials mentioned in the article were converted to reversible hydrogen electrode scale (RHE) without *iR* correction [7]. The scan rate was 5 mV/s and voltage range from -0.9 to -1.5 V for the linear sweep voltammetry (LSV) measurements, followed by 20 cycles of the cyclic voltammogram (CV) to activate the samples and make sure the working electrodes steady. The double-layer capacitance (C_{dl}) was linearly related to the electrochemical surface area (ECSA) according to the equation: ECSA $= C_{dl}/C_S$

(C_S =0.060 mF/cm^2) [31, 32]. The cyclic voltammetry (CV) was conducted in the potential window of -0.6 ~ -0.7 V at various scan rate of 20, 40, 60, 80 and 100 mV/s. The electrochemical impedance spectroscopy (EIS) were conducted with frequency ranging from 100,000 Hz to 1 Hz. Long-term stability of HER was measured by chronoamperometry at a constant potential of 200 mV for 15 h in 1M KOH.

3. RESULTS AND DISCUSSION

3.1 SEM and TEM Analysis of WTe$_{2-x}$/CC

The SEM image in Figure 2a displays that the WO$_3$ grown on carbon cloth (WO$_3$/CC) is pinion-like structure, which agglomerates to gearwheel-like structure after tellurization (WTe$_2$/CC), seen in Figure 2b. After WTe$_2$/CC is annealed at 80, 100°C, there is no noticeable variation in the morphology shown in Figure 2c and 2d. However, when the annealing temperature is raised to 200°C, the gearwheel-like morphology of WTe$_{2-x}$/CC is destroyed, shown in Figure 2e. Furthermore, when the annealing temperature is further raised to 300°C, the gearwheel-like structure of WTe$_{2-x}$ collapses and bulks appear, in Figure 2f.
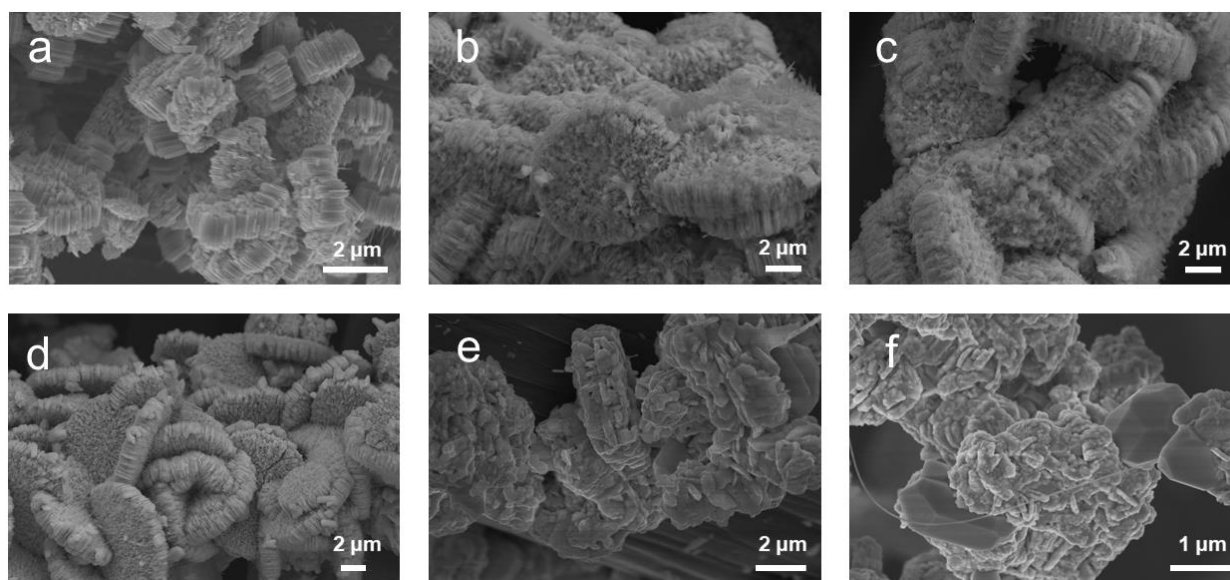

Figure 2. SEM images: (a) WO$_3$/CC; (b) WTe$_2$/CC; WTe$_{2-x}$/CC annealed at (c) 80°C, (d) 100°C, (e) 200°C and (f) 300°C.

To examine the composition of WTe$_{2-x}$/CC, the energy dispersive X-ray spectroscopy (EDS) was executed, as shown in Figure 3. The mapping shows the elements of W, Te and C uniformly distributed over the whole surface. The energy spectrum analysis of SEM displays that the element ratios of Te:W in WTe$_{2-x}$/CC annealed at 80°C, 100°C, 200°C, 300°C was 1.870:1, 1.661:1, 1.651:1, 1.642:1 respectively, all lower than the atomic ratio of 2:1 in the chemical formula, indicating that the Te vacancies can be introduced by annealing in vacuum. When the temperature was raised from 80°C to

100°C, the quantity of Te vacancy was increased gradually and kept at an almost constant Te:W atomic ratio at the annealing temperature of 100°C, 200°C and 300°C.
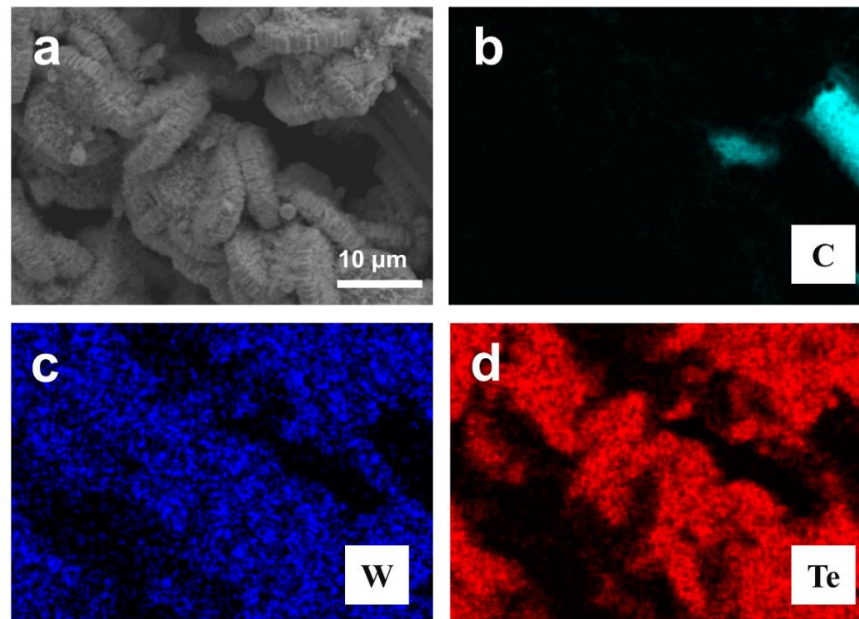

Figure 3. (a) Morphology image of WTe$_{2-x}$/CC annealed at 100°C and the corresponding EDS mappings of (b) C, (c) W and (d) Te element.

3.2 XRD and Raman Analysis of WTe$_{2-x}$/CC

WO$_3$/CC, WTe$_2$/CC and WTe$_{2-x}$/CC are investigated by X-ray diffraction (XRD) shown in Figure 4a and 4b. Except for the peaks derived from carbon cloth, the other strong and sharp peaks match well with WO$_3$ and WTe$_2$ respectively.
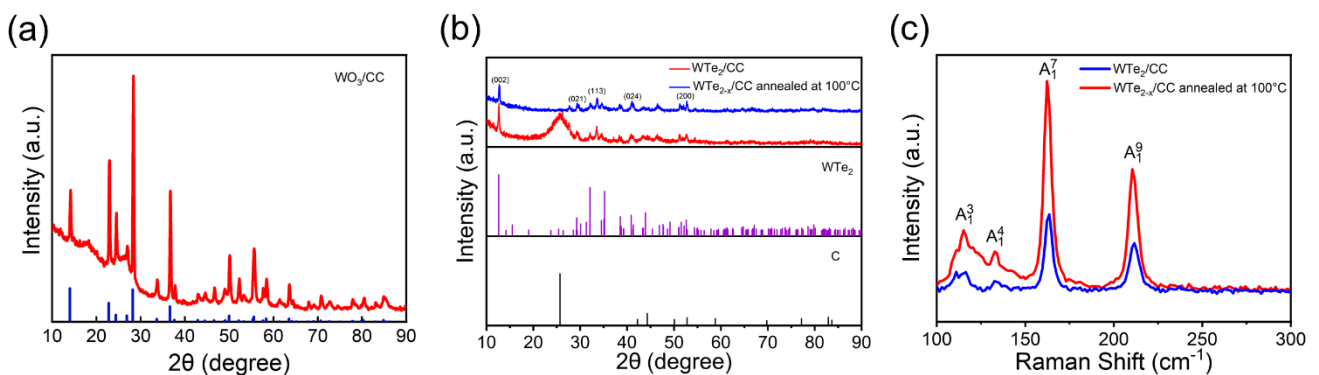

Figure 4. XRD patterns of (a) WO$_3$/CC, (b) WTe$_2$/CC and WTe$_{2-x}$/CC. (c) Raman spectra of WTe$_2$/CC and WTe$_{2-x}$/CC.

The diffraction peaks at 12.62°, 29.26°, 35.21°, 38.57°, and 52.60° represent the (0 0 2), (0 2 1), (1 1 3), (0 2 4), and (2 0 0) crystal planes of WTe$_2$ respectively. Moreover, there are no impurity peaks

after introducing Te vacanies. Raman spectroscopy characterization in Figure 4c shows the characteristic modes for the 100~300 cm^{-1} region. Both samples demonstrate four main peaks at about 118, 134, 164, 212 cm^{-1} corresponding to A_1^3, A_1^4, A_1^7, A_1^9 modes of WTe_2 respectively [20, 33], whether introducing Te vacanies or not.

3.3 XPS and EPR Analysis of WTe$_{2-x}$/CC

To dissect the molecular structure information of WTe$_{2-x}$/CC, high-resolution XPS analysis was conducted either before and after the in-situ vacuum annealing at 100°C. As shown in Figure 5a, The W 4f peak of WTe$_{2-x}$/CC shifted negatively by 0.70 eV compared with WTe$_2$/CC, while the Te 3d peaks stay changeless after introducing Te vacancies. Given that W atoms are surroundingly packed by Te atoms to constitute octahedral strcture, the Te vacancies will influence the chemical state of W 4f nearby but scarcely altered the chemical state of Te 3d [20, 33]. The Te deficiency may act as the active sites for HER and contribute to improve the HER electrocatalytic activity.
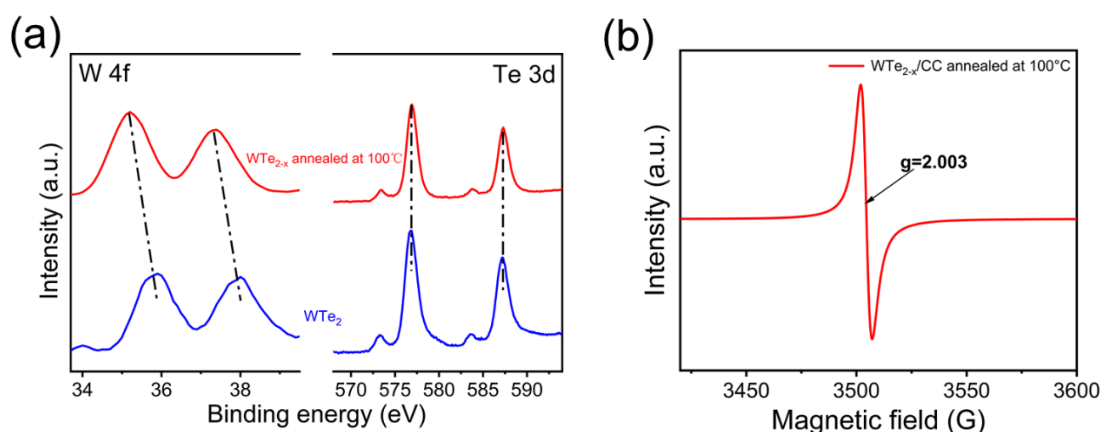

Figure 5. (a) XPS spectra of WTe$_2$/CC and WTe$_{2-x}$/CC annealed at 100°C. (b) EPR spectra of WTe$_{2-x}$/CC annealed at 100°C.

According to the energy spectrum analysis in 3.1, Te vacancies of WTe$_{2-x}$/CC is rich after annealed in vacuum at 100°C. Electron paramagnetic spin resonance (EPR) used to capture the presence of unpaired electron by magnetic moment change signal of spectra is performed on WTe$_{2-x}$/CC annealed at 100°C, shown in Figure 5b. Te vacancy is definitely a point defect of Te atom, so, for the absence of Te atom, there must be unpaired electrons at the defect. Therefore, the dimensionless factor g=2.003 of WTe$_{2-x}$/CC obtained by EPR test indicates the existence of Te vacancies.

3.4 Electrochemical Performance of WTe$_{2-x}$/CC

To examine the impact of Te vacanies on the HER catalytic activity, WTe$_{2-x}$/CC catalysts were measured in 1.0 M KOH electrolyte of a three-electrode cell, with WO$_3$/CC, WTe$_2$/CC and commercial Pt/C tested as the references.
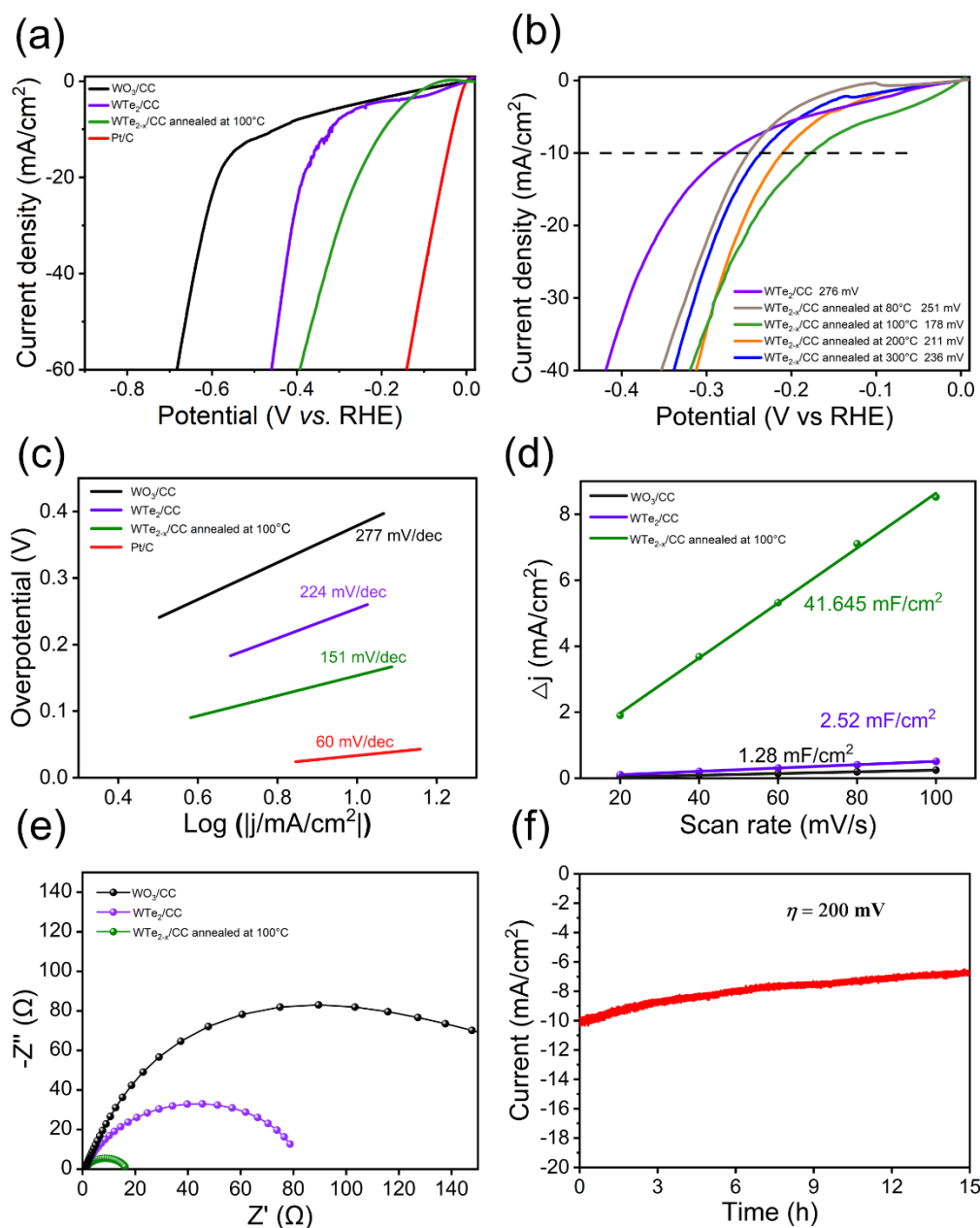
Figure 6. HER electrocatalytic activity of different samples. Polarization curves of (a) WO$_3$/CC, WTe$_2$/CC, Pt/C, WTe$_{2-x}$/CC annealed at 100°C and (b) WTe$_{2-x}$/CC annealed at different temperature. (c) Tafel plots of WO$_3$/CC, WTe$_2$/CC, WTe$_{2-x}$/CC, and Pt/C at a scan rate of 5 mV/s. (d) Estimated C_{dl} values and (e) EIS plots of WO$_3$/CC, WTe$_2$/CC and WTe$_{2-x}$/CC. (f) Amperometric *i-t* curves with an applied voltage of 200 mV vs. RHE in 1.0 M KOH.

The linear sweep voltammetry (LSV) polarization curves were present in Figure 6a and 6b. The WTe$_{2-x}$/CC annealed at 100°C exhibits the best HER catalytic activity with 178 mV overpotential at the current density of 10 mA/cm^2, outperforms that of WO$_3$/CC (451 mV), WTe$_2$/CC (327 mV) and WTe$_{2-x}$/CC annealed at other temperatures. The enhanced catalytic property may originate from the exposure of more active sites caused by Te vacancies after thermal reduction in vacuum. When the annealing temperature ranges from 80°C to 100°C, the overpotential decreases may due to the intensive number of

Te vacancies and the increased active sites. When the temperature is higher than 100°C, the quantity of Te vacancy stays a constant, however the morphology aggregates collapse, which leads to the diminution of active sites and weakens the catalytic activity of hydrogen evolution. To sum up, WTe_{2-X}/CC annealed at 100°C performs best in alkaline HER.
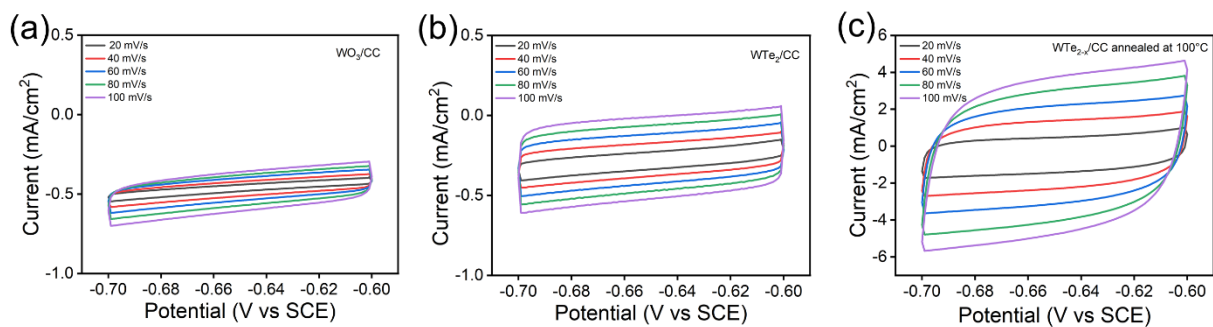

Figure 7. CV curves of samples: (a) WO_3/CC, (b) WTe_2/CC and (c) WTe_{2-x}/CC annealed at 100°C in the region of -0.7 ~ -0.6 V vs. RHE.

Table 1. Comparison with similar HER electrocatalysts described in other literatures.

Materials	Tafel slope (mV/dec)	η (mV *vs.* RHE)	Electrolyte	Ref.
1T-2H MoS_2	65	320 (10 mA/cm^2)	1M KOH	34
Te-WS_2	94	213 (10 mA/cm^2)	1M KOH	35
NiS_2-MoS_2	65	204 (10 mA/cm^2)	1M KOH	36
WTe_{2-x}/CC	151	178 (10 mA/cm^2)	1M KOH	This work
MoS_2/NiS_3	83	110 (10 mA/cm^2)	1M KOH	37
N-ReS_2	85	90 (10 mA/cm^2)	1M KOH	8
$W_{1-x}Te_2$	94	251 (10 mA/cm^2)	1M KOH	29

To further explore the HER kinetics of WTe_{2-x}/CC, Tafel slope plots are shown in Figure 6c. The Tafel slope of WTe_{2-x}/CC is 151 mV/dec, which means that introducing Te vacanies results in the beneficial HER kinetics. Besides, considering that ECSA is proportionate to the double-layer capacitance (C_{dl}), C_{dl} was quantitatively estimated by CV with scan rates of 20, 40, 60, 80, and 100 mV/s when potential range from -0.6 to -0.7 V (Figure 6d and Figure 7). The C_{dl} of WTe_{2-x}/CC was evaluated to be 41.645 mF/cm^2, which is much higher than that of other samples (WTe_2: 2.52 mF/ cm^2, WO_3: 1.28 mF/cm^2), thus to qualitatively estimate ECSA by this mean. It can be concluded that Te deficiency activates WTe_{2-x}/CC matrix, which is propitious to the HER process. Meanwhile the electrochemical impedance spectroscopy (EIS) is conducted to study the charge-transfer ability during alkaline HER process. As shown in Figure 6e, the charge transfer resistance (R_{ct}) of WTe_{2-x}/CC (8 Ω) is dramatically lower than that of WTe_2/CC (40 Ω), demonstrating an accelerated electron transfer kinetics of the WTe_2-

$_x$/CC catalyst in HER reaction. Furthermore, the long-cycle stability of WTe$_{2-x}$/CC was investigated using amperometric *i-t* curve with overpotential of 200 mV. As shown in Figure 6f, it maintains a steady HER activity after continuous operation for 15 h, which indicates WTe$_{2-x}$/CC has a superior stability.

Furthermore, we also make the comparison with similar HER electrocatalysts described in other literatures. As shown in Table 1, the red one is the WTe$_{2-x}$/CC in our work, delivering a highly electrochemistry HER activity.

4. CONCLUSION

In summary, we have constructed WTe$_{2-x}$ with gear-like morphology grown on conductive carbon cloth by hydrothermal method, telluride treatment and sequential annealing in vacuum. The WTe$_{2-x}$/CC with Te vacancies exposes an ameliorative overpotential from 327 mV to 178 mV and a Tafel slope of 151 mV/dec in the alkaline HER. The reduced charge transfer resistance with electrolyte and the enlarged electrochemical active surface area in Te-deficient WTe$_{2-x}$/CC can contribute to the more excellent HER performance than pristine WTe$_2$/CC.

CONFLICTS OF INTEREST
There are no conflicts to declare.

References

1. M. Conte, M. Ronchetti, R. Vellone, *J. Power Sources*, 100 (2001) 171-187.
2. N. Lior, *Energy Convers. Manage.*, 43 (2002) 1187-1198.
3. M.S.D.I.L. Thomas, *Nature*, 414 (2001) 332-337.
4. P. Nikolaidis, A. Poullikkas, *Renewable Sustainable Energy Rev.*, 67 (2017) 597-611.
5. R.W. Howarth, M.Z. Jacobson, *Energy Sci. Eng.*, 9 (2021) 1676-1687.
6. L. Tian, X. Zhai, X. Wang, J. Li, Z. Li, *J. Mater. Chem. A*, 8 (2020) 14400-14414.
7. K. Xu, H. Ding, M. Zhang, M. Chen, Z. Hao, L. Zhang, C. Wu, Y. Xie, *Adv. Mater.*, 29 (2017) 1606980.
8. Q. Sun, B. Zhang, L. Diao, B. Chen, K. Song, L. Ma, F. He, *J. Mater. Chem. A*, 8 (2020) 11607-11616.
9. Z. Zhao, H. Liu, W. Gao, W. Xue, Z. Liu, J. Huang, X. Pan, Y. Huang, *J. Am. Chem. Soc.*, 140 (2018) 9046-9050.
10. B. Zhang, H. Qin, Y. Pan, W. Lin, S. Xu, Q. Sun, E. Liu, F. He, L. Diao, C. He, L. Ma, *ACS Appl. Nano Mater.*, 4 (2020) 372-380.
11. Y. Jiao, Y. Zheng, M. Jaroniec, S.Z. Qiao, *Chem. Soc. Rev.*, 44 (2015) 2060-2086.
12. J. Huang, J. Han, T. Wu, K. Feng, T. Yao, X. Wang, S. Liu, J. Zhong, Z. Zhang, Y. Zhang, B. Song,

   ACS Energy Lett., 4 (2019) 3002-3010.
13. Y. Zhao, T. Ling, S. Chen, B. Jin, A. Vasileff, Y. Jiao, L. Song, J. Luo, S.Z. Qiao, *Angew Chem. Int. Ed. Engl.*, 58 (2019) 12252-12257.
14. R. Subbaraman, D. Tripkovic, K.C. Chang, D. Strmcnik, A.P. Paulikas, P. Hirunsit, M. Chan, J. Greeley, V. Stamenkovic, N.M. Markovic, *Nat. Mater.*, 11 (2012) 550-557.
15. C. Huang, B. Zhang, Y. Wu, Q. Ruan, L. Liu, J. Su, Y. Tang, R. Liu, P.K. Chu, *Appl. Catal., B*, 297 (2021) 120461.
16. R. Lv, J.A. Robinson, R.E. Schaak, D. Sun, Y. Sun, T.E. Mallouk, M. Terrones, *Acc Chem Res*, 48 (2015) 56-64.
17. L. Lin, P. Sherrell, Y. Liu, W. Lei, S. Zhang, H. Zhang, G.G. Wallace, J. Chen, *Adv. Energy Mater.*, 10 (2020) 1903870.
18. M. Chhowalla, H.S. Shin, G. Eda, L.J. Li, K.P. Loh, H. Zhang, *Nat. Chem.*, 5 (2013) 263-275.
19. C. Xiao, R. Sa, Z. Cui, S. Gao, W. Du, X. Sun, X. Zhang, Q. Li, Z. Ma, *Appl. Surf. Sci.*, 563 (2021) 150388.
20. H. Kwon, B. Ji, D. Bae, J.H. Lee, H.J. Park, H. Kim, Y.M. Kim, Y.W. Son, H. Yang, S. Cho, *Appl. Surf. Sci.*, 515 (2020) 145972.
21. N. Ling, S. Zheng, Y. Lee, M. Zhao, E. Kim, S. Cho, H. Yang, *APL Mater.*, 9 (2021) 061108.
22. L. Lin, N. Miao, Y. Wen, S. Zhang, P. Ghosez, Z. Sun, D.A. Allwood, *ACS Nano*, 10 (2016) 8929-8937.
23. S.S. Chou, N. Sai, P. Lu, E.N. Coker, S. Liu, K. Artyushkova, T.S. Luk, B. Kaehr, C.J. Brinker, *Nat. Commun.*, 6 (2015) 8311.
24. J.M. Woods, D. Hynek, P. Liu, M. Li, J.J. Cha, *ACS Nano*, 13 (2019) 6455-6460.
25. J. Xia, D.F. Li, J.D. Zhou, P.Yu, J.H. Lin, J.L. Kuo, H.B. Li, Z. Liu, J.X. Yan, Z.X. Shen, *Small*, 13 (2017) 1701887.
26. S. Kim, S. H. Jhi, *Appl. Phys. Lett.*, 110 (2017) 263104.
27. H. Wang, L. Ouyang, G. Zou, C. Sun, J. Hu, X. Xiao, L. Gao, *ACS Catal.*, 8 (2018) 9529-9536.
28. A. Eftekhari, *J. Mater. Chem. A*, 5 (2017) 18299-18325.
29. X. Wang, J. Wang, B. Wei, N. Zhang, J. Xu, H. Miao, L. Liu, C. Su, Y. Li, Z. Wang, *J. Mater. Sci. Technol.*, 78 (2021) 170-175.
30. S. Yao, X. Zheng, X. Zhang, H. Xiao, F. Qu, X. Wu, *Mater. Lett.*, 186 (2017) 94-97.
31. Q. Liang, L. Zhong, C. Du, Y. Luo, J. Zhao, Y. Zheng, J. Xu, J. Ma, C. Liu, S. Li, Q. Yan, *ACS Nano*, 13 (2019) 7975-7984.
32. C.C. McCrory, S. Jung, I.M. Ferrer, S.M. Chatman, J.C. Peters, T.F. Jaramillo, *J. Am. Chem. Soc.*, 137 (2015) 4347-4357.
33. Y. Kim, Y.I. Jhon, J. Park, J.H. Kim, S. Lee, Y.M. Jhon, *Nanoscale*, 8 (2016) 2309-2316.
34. S. Wang, D. Zhang, B. Li, C. Zhang, Z. Du, H. Yin, X. Bi, S. Yang, *Adv. Energy Mater.*, 8 (2018) 1801345.
35. Y. Pan, F. Zheng, X. Wang, H. Qin, E. Liu, J. Sha, N. Zhao, P. Zhang, L. Ma, *J. Catal.*, 382 (2020) 204-211.
36. P. Kuang, T. Tong, K. Fan, J. Yu, *ACS Catal.*, 7 (2017) 6179-6187.
37. J. Zhang, T. Wang, D. Pohl, B. Rellinghaus, R. Dong, S. Liu, X. Zhuang, X. Feng, *Angew. Chem. Int. Ed.*, 55 (2016) 6702.